Check for updates

From molecular architecture to environmental action: a new palladium-based perovskite catalyst as a cathodic modifier for electro-Fenton degradation

Houyem Khlifi,[a] Ahlem Guesmi,[b] Nejmeddine Rabaaoui, [ID][a] Mourad Cherif,[c] Noureddine Mhadhbi,[a] Wesam Abd El-Fattah,[b] Naoufel Ben Hamadi[b] and Houcine Naïli [ID] *[a]

A new one-dimensional (1D) palladium-based hybrid perovskite, $(C_9H_8N)[PdCl_3(H_2O)]$, has been synthesized and structurally characterized, revealing a distinctive asymmetric architecture with two non-equivalent formula units ($Z' = 2$). The compound exhibits a see–saw coordination geometry around Pd(II), stabilized through a network of hydrogen bonds, π–π stacking, and halogen–halogen interactions, which collectively enhance its structural robustness and functional properties. Beyond its architectural novelty, the material demonstrated excellent catalytic activity as a cathodic modifier in a Boron-Doped Diamond (BDD)-assisted electro-Fenton system for paraquat degradation. The hybrid-modified electrode significantly accelerated the degradation process, achieving near-complete mineralization under optimized conditions. This study highlights the potential of $(C_9H_8N)[PdCl_3(H_2O)]$ as a multifunctional material that bridges structural design with environmental application, offering valuable insights into the development of advanced hybrid perovskites for sustainable pollutant remediation.

Introduction

Hybrid metal-halide perovskites represent a rapidly evolving class of materials that have garnered widespread attention due to their structural tunability and multifunctional properties. Traditionally investigated for their performance in optoelectronics and photovoltaics, these compounds have more recently gained recognition for their potential in catalysis and environmental remediation.[1–4] Their intrinsic modularity, which allows for the rational incorporation of both organic and inorganic components, offers unique avenues to design low-dimensional architectures with tailored chemical and physical behavior.

Within this domain, the development of palladium-based hybrid perovskites remains significantly underexplored, despite the well-established coordination chemistry and catalytic relevance of Pd(II) complexes.[5–7] The ability of palladium to adopt diverse coordination environments and mediate redox processes makes it an attractive yet underutilized candidate for constructing functional hybrid frameworks. Particularly, one-dimensional (1D) Pd-based systems stabilized by non-covalent

interactions such as hydrogen bonding, π–π stacking, and halogen contacts present a promising platform for investigating structure–property relationships in emerging catalytic materials.[8–10]

Although recent efforts have been devoted to tin- and lead-based hybrid perovskites for optoelectronic and photocatalytic applications,[11–13] there is a conspicuous lack of systematic studies addressing Pd-based analogues, especially those linking precise structural features with catalytic performance. Moreover, structural asymmetry within the crystal lattice—manifested through non-equivalent formula units and variable local coordination—remains an under-investigated parameter that could profoundly influence material stability, charge transport, and reactivity under external stimuli.[14,15]

At the same time, the integration of hybrid perovskite materials into electrochemical technologies for environmental remediation is gaining momentum. The Electro-Fenton (EF) process, in particular, benefits from the development of advanced cathodic materials that can efficiently promote H_2O_2 generation and facilitate iron redox cycling. While boron-doped diamond (BDD) electrodes have demonstrated excellent electrochemical stability, their functional performance can be significantly enhanced through surface modification with catalytically active materials. In this regard, the use of structurally defined hybrid perovskites—especially those based on

[a]*Laboratory Physical-Chemistry of the Solid State, Department of Chemistry, Faculty of Sciences of Sfax, University of Sfax, BP 1171, 3000 Sfax, Tunisia. E-mail: houcine_naili@yahoo.com; houcine.naili@fss.rnu.tn*

[b]*Chemistry Department, College of Science, Imam Mohammad Ibn Saud Islamic University (IMSIU), P. O. Box 5701, Riyadh 11432, Saudi Arabia*

[c]*Laboratoire de Physico-chimie des Matériaux, IPEST, BP51, 2070 La MARSA, Tunisia*

Pd(II)—as electrode modifiers for pollutant degradation remains largely unreported.

In light of these considerations, the present study focuses on the synthesis and comprehensive characterization of a novel one-dimensional Pd-based hybrid perovskite, $(C_9H_8N)[PdCl_3(H_2O)]$. The structural features of this material, including its asymmetric crystallographic motif and network of stabilizing interactions, are examined in detail. Furthermore, its application as a cathodic modifier in a BDD-assisted electro-Fenton system is investigated using paraquat as a model pollutant. This work aims to elucidate the relationship between molecular-level architecture and macroscopic catalytic behavior, thereby contributing to the rational design of multifunctional hybrid materials for sustainable environmental technologies.

Experimental section

Chemical materials and synthesis

The title compound was synthesized using analytical-grade reagents, all of which were used as received from commercial suppliers (Sigma-Aldrich), while distilled water served as the solvent for all syntheses. To ensure the formation of high-quality crystals, the starting materials were purified through recrystallization prior to use. The reaction involved 1 mmol (0.177 g) of palladium chloride, 2 mmol (0.258 g) of quinoline (C_9H_7N), and 10 mL of distilled water. The mixture was acidified with concentrated hydrochloric acid (0.080 g) and stirred continuously. After several days of slow evaporation, colorless, block-shaped crystals of the target salt were obtained. Elem. Microanal. Obsd for $(C_9H_8N)[PdCl_3(H_2O)]$ (calcd): C, 11.66 (11.41); H, 2.42 (2.24); N, 8.32 (8.09). (IR, KBr, cm^{-1}): $\nu(H_2O)$, 3405 s; $\nu(N–H^+)$, 1521 m; $\nu(C–N)$, 1650 m, (s: strong, m: medium). The yield of the reaction was 0.701 g (97%). ESI/MS m/z [M–H]-calcd 721.56, found 721.86.

X-ray diffraction analysis

A single crystal, approximately $0.30 \times 0.12 \times 0.09$ mm^3, was used to collect diffraction data at 100 K with an Xcalibur Atlas Gemini Ultra diffractometer utilizing Mo-Kα radiation ($\lambda = 0.71073$ Å) and processed through the SCALE3 ABSPACK[16] program. Data collection, reduction, and analysis were conducted using SAINT, with semi-empirical multi-scan absorption corrections applied via the SADABS[17] program. The crystal structure was determined in the monoclinic space group $P2_1/c$ using auto-methods available in WINGX.[18] The structure of $(C_9H_8N)[PdCl_3(H_2O)]$ was solved by the dual-space algorithm using SHELXT-2015 (ref. 19) and refined by full-matrix least-squares techniques using SHELXL[20] with anisotropic thermal parameters for all non-hydrogen atoms. All figures were prepared using DIAMOND.[21] The refinement conditions and structural resolution of our compound are outlined in Table S1.

Spectroscopic study

FTIR measurements were carried out at room temperature using a PerkinElmer Spectrum 400 spectrometer equipped with a universal attenuated total reflectance (UATR) sensor, covering the 400–4000 cm^{-1} spectral range. Raman spectra were recorded at ambient conditions over 50–3500 cm^{-1} using a Thermo Fisher DXR Raman spectrometer.

Thermal analysis

The thermal decomposition behavior of the $(C_9H_8N)[PdCl_3(H_2O)]$ complex was examined through simultaneous thermogravimetric analysis (TGA) and differential Scanning Calorimetry (DSC) under a nitrogen atmosphere (flow rate: 100 mL min^{-1}) using a SETARAM TG-DSC 92 instrument. The analysis was performed on a 2.687 mg sample, with thermograms recorded over a temperature range of 25–400 °C for DSC and TGA, applying a constant heating rate of 10 °C min^{-1} (Fig. 6).

Application in paraquat herbicide degradation

Electrodes preparation. BDD films were provided by CSEM and synthesized on a conductive p-Si substrate (1 mm, Siltronix) via a hot filament, chemical vapor deposition technique (HF-CVD). The temperature of the filament was from 2440 to 2560 °C and that of the substrate was monitored at 830 °C. The reactive gas used was 1% methane in hydrogen-containing 1–3 ppm of trimethyl boron. The gas mixture was supplied to the reaction chamber at a flow rate of 5 L min^{-1} to give a growth rate of 0.24 μm h^{-1} for the diamond layer. This procedure gave a columnar, randomly textured, polycrystalline diamond film, with a thickness of about 1 μm and a resistivity of 15 mΩ cm ($\pm$30%) onto the conductive p-Si substrate.[22]

A glassy carbon electrode (GCE, 3 mm diameter) was used as the cathodic substrate. Prior to modification, the electrode was polished sequentially with alumina slurry (0.05 μm), rinsed thoroughly with deionized water and ethanol, and dried under nitrogen flow. A homogeneous catalyst ink was prepared by ultrasonically dispersing 5 mg of the synthesized $(C_9H_8N)[PdCl_3(H_2O)]$ complex in a mixture of 450 μL ethanol, 450 μL deionized water, and 100 μL Nafion® 5 wt%. The suspension was sonicated for 30 minutes to ensure homogeneity. Then, 7 μL of the ink was dropped-casted onto the GCE surface and dried at 60 °C for 30 minutes to form a uniform catalytic film. The modified electrode was stored in a desiccator until use.

Chemicals and electrolytes. Sodium sulfate (Na$_2$SO$_4$, ACS reagent, $\geq$99.0%), paraquat (99.8%), sodium chloride (NaCl, $\geq$99.5%), sodium hydroxide (NaOH, $\geq$98.0%), and methanol (CH$_3$OH, $\geq$99.9%) were supplied by Sigma-Aldrich and were used as received without purification. Deionized water from a Millipore Milli-Q system (resistivity > 18 MΩ cm) was used for the preparation of aqueous solutions.

Monopyridone, dipyridone, 4-carboxy-1-methylpyridinium, 4-picolinic acid, 4,4′-bipyridyl, oxalic acid, malic acid, succinic acid, formic acid, citric acid, acrylic Acid, glyoxylic acid, and glycolic acid (as standards) were of analytical grade, and they were purchased from Sigma-Aldrich. These products were used to identify the by-products of paraquat's degradation; the chemical structure of paraquat is outlined in Table S7.

Electro-Fenton galvanostatic degradation of paraquat. Electro-Fenton treatments were performed at room temperature

(25 $\pm$ 2 °C) in a 250 mL single-compartment glass cell under continuous magnetic stirring and aeration. The electrolysis was conducted under galvanostatic conditions using a two-electrode configuration powered by a regulated DC power supply. A boron-doped diamond plate (2.5 × 4 cm²) was used as the anode, while the cathode consisted of a glassy carbon electrode (GCE, 3 mm diameter) modified with a thin film of the synthesized hybrid perovskite (C_9H_8N)[$PdCl_3(H_2O)$]. The supporting electrolyte consisted of 50 mmol·L^{-1} Na$_2$SO$_4$, and Fe^{2+} ions (0.2 mmol·L^{-1} as FeSO$_4$·7H$_2$O) were added to initiate the Fenton reaction. The initial concentration of paraquat was fixed at 30 mg·L^{-1}, and the pH of the solution was adjusted to 3.0 using diluted H$_2$SO$_4$. The interelectrode distance was maintained at approximately 2 cm. Galvanostatic current densities ranging from 10 to 30 mA·cm^{-2} were applied to assess the influence of current intensity on the degradation kinetics and mineralization efficiency. During the reaction, voltage and current were monitored in real time using a digital multimeter. Aliquots (2 mL) were sampled at specific intervals (0, 15, 30, 60, 90, and 120 min), filtered through 0.22 µm membranes, and immediately analyzed.

Analytical determinations. Solutions were prepared using distilled water. The temperature was maintained using a thermostatically controlled water bath. The current density was obtained using a Bench Power Supply GPC-3030D potentiostat-galvanostat. Chemical oxygen demand (COD) data were obtained with a Beckman UV/Vis DU 800 spectrophotometer. The total organic carbon content (TOC) was obtained with a Shimadzu VCSH TOC analyzer. For this, samples were withdrawn and filtred through a millipore syringe filter of 0.45 µm and aliquots of 50 µL were injected into the analyzer. The concentration of paraquat and reaction intermediates were determined by a Spectra SYSTEM HPLC-Thermo Fisher Scientific equipped with a diode array detector (DAD) detector. A ZORBAX Eclipse XDB-C18 reverse phase column (150 mm, 4.6 mm, 5 µm) was used for the quantification of paraquat and aromatic intermediates. HPLC measurements were conducted by injecting aliquots of 20 µL into the chromatograph. A mixture of water and methanol (70 : 30 v/v) was used as mobile phase at 0.8 mL min^{-1} as throughput in isocratic mode. For kinetic studies, the detection was performed at 230 nm.

Results

Structural architecture

Fig. 1 presents the asymmetric unit of the newly synthesized 1D Pd-based metal-halide hybrid perovskite, which diverges from the conventional norm by incorporating two crystallographically independent formula units ($Z' = 2$) within the same unit cell. This structural anomaly signifies the presence of subtle yet meaningful disparities in the local coordination environments and bond metrics across the two PdCl$_3$(H$_2$O) subunits. The compound crystallizes in the monoclinic crystal system, specifically within the $P2_1/c$ space group, which permits the accommodation of such internal asymmetry without compromising the global lattice coherence.
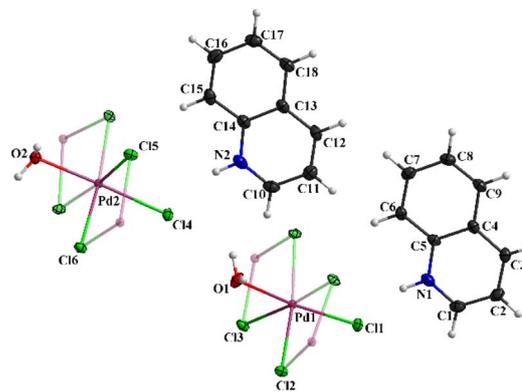

Fig. 1 Asymmetric unit of the titled compound completed by symmetry.

In this figure, transparency is used to emphasize the distorted see–saw geometry of the PdCl$_3$(H$_2$O) coordination unit, a configuration that governs the connectivity and topology of the extended one-dimensional chain. The distinction between the Pd1 and Pd2 centers is clearly observable, each coordinated by three chloride ligands and one water molecule, yet displaying slight but systematic differences in bond lengths and angles. These variations, though seemingly minor, are structurally significant and collectively necessitate a Z' of 2, a relatively rare occurrence in perovskite-like frameworks, where higher internal symmetry ($Z' = 1$ or 0.5) is typically favored.

The existence of two distinct formula units implies a locally asymmetric landscape within the crystalline matrix, which may have far-reaching consequences on both stability and material functionality. Such a configuration could, for instance, promote a more robust thermomechanical behavior or lead to modulated electronic environments, with subtle shifts in orbital overlap and electron distribution that might influence the band gap or charge transport properties. These effects are especially relevant in hybrid metal-halide systems, where even small perturbations at the atomic scale can produce measurable changes in macroscopic behavior.

Moreover, the directional nature of the Pd–Cl and Pd–O bonding within the see–saw geometry plays a crucial role in facilitating the formation of the extended 1D inorganic backbone. This spatial orientation also allows for the possibility of supramolecular interactions such as hydrogen bonding, halogen···halogen contacts, and π···π stacking between adjacent chains, thereby contributing to both structural stabilization and functional tunability.

A full summary of the crystallographic metrics, including unit cell dimensions, atomic coordinates, and geometric parameters, is provided in Table S1.

Fig. 2 illustrates the key structural distinctions between the two non-equivalent formula units in the asymmetric unit of the 1D Pd-based hybrid perovskite ($Z' = 2$).

In panel A, the coordination environments of the two Pd(II) centers (Pd1 and Pd2) are shown, each adopting a distorted see–saw geometry with three chloride ligands and one coordinated water molecule. Notably, the Pd–Cl and Pd–O bond lengths
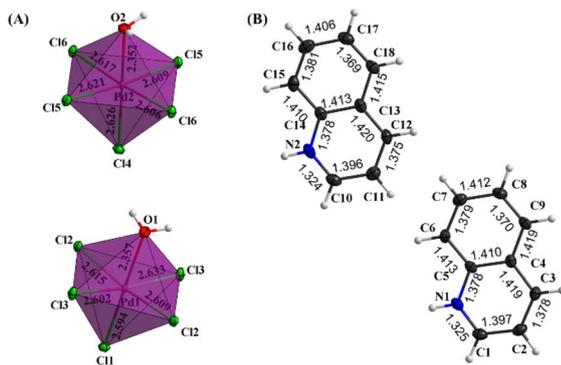
Fig. 2 Bond discrepancies between the two formula units in the asymmetric unit.

Fig. 3 Projections of the unit cell along the (A): b-axis, (B): c-axis, (C): a-axis.

differ slightly between the two units, with Pd1 ranging from 2.524 to 2.634 Å and Pd2 displaying comparable but distinct values. These subtle variations underscore the asymmetric environment and suggest localized differences in steric or hydrogen bonding effects. Such non-equivalence contrasts with the uniform square-planar geometries typically observed in symmetric 2D Pd halide perovskites like $[(CH_3)_2NH_2]_2PdBr_4$ and $(CH_3NH_3)_2PdCl_4$, where Pd–X bonds are nearly identical.[23],[24]

Panel B focuses on the quinolinium cations, revealing minor but meaningful differences in the aromatic framework. Specifically, variations in C–N and C–C bond lengths near the protonated nitrogen centers (N1 and N2) indicate altered π-electron distribution between the two organic components. These discrepancies suggest localized differences in hydrogen bonding or packing stress, which may influence the stacking interactions, vibrational behavior, and electronic distribution across the structure.

The combined structural distortions, both in the inorganic coordination sphere and the organic framework, validate the Z' = 2 configuration. This level of asymmetry, while uncommon in simpler perovskite systems, has been observed in low-dimensional Pd complexes and is often linked to unique optical or conductive properties.[25]

The bond metrics presented in Table S4 further confirm these observations, offering detailed comparisons of bond angles and lengths that define the structural complexity of the system.

Fig. 3 illustrates three orthogonal projections of the unit cell for the 1D Pd-based metal-halide hybrid perovskite, offering a comprehensive understanding of the spatial distribution of its organic and inorganic components.

In panel A (view along the b-axis), the $[PdCl_3(H_2O)]^-$ units are seen forming extended one-dimensional chains through edge-sharing chloride ligands. These chains are aligned in parallel and are separated by organic quinolinium cations, which intercalate between the inorganic subunits and contribute to structural cohesion through hydrogen bonding and electrostatic interactions.

Panel B (view along the c-axis) emphasizes the layered stacking arrangement, where the aromatic organic cations form ordered planes between the inorganic chains. This
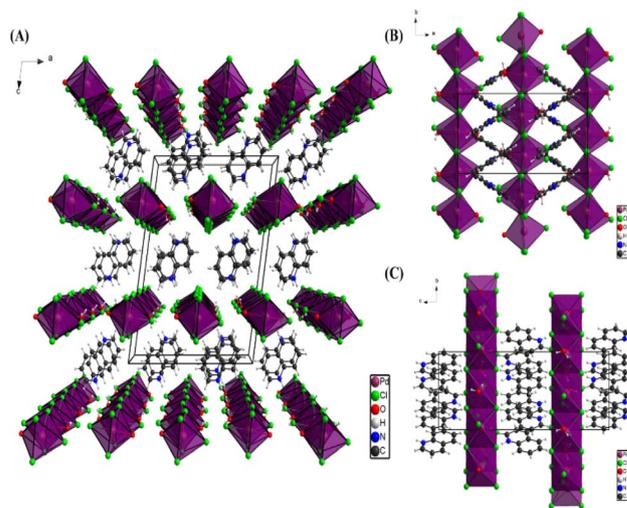
configuration highlights the likelihood of π–π stacking between the quinolinium rings, which enhances lattice stability and may facilitate interchain electronic communication. Such ordered aromatic layers are not typically observed in previously reported Pd(II) perovskites, such as those based on methylammonium or dimethylammonium cations.[23],[25]

In Panel C (view along the a-axis), the repeating alternation of organic and inorganic domains is clearly visible, showing the uniform encapsulation of the $PdCl_3(H_2O)$ chains within an organic matrix. This hybrid configuration creates a directional framework that may influence the optical anisotropy and electronic transport properties of the material. Compared to the 2D layered structures in $[(CH_3)_2NH_2]_2PdBr_4$ and $(CH_3NH_3)_2$-$PdCl_4$,[23],[24] this 1D configuration represents a more spatially constrained architecture with distinct physicochemical behavior.

Fig. 4 illustrates the intricate interplay of hydrogen bonding and halogen–halogen interactions between the organic and
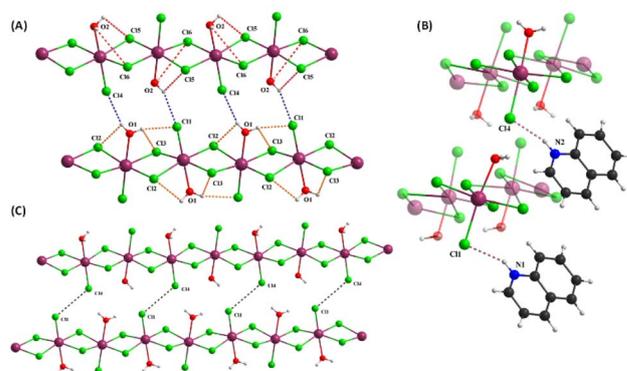

Fig. 4 (A) Three-dimensional crystal packing of $(C_9H_8N)[PdCl_3(H_2O)]$. (B) Projection of the structure along the [010] direction. (C) View highlighting the halogen–halogen interactions stabilizing the crystal packing.

inorganic components, as well as within the inorganic 1D chain itself. These non-covalent interactions are crucial in stabilizing the overall structure and influencing the material's properties. Table S5 provides the distances and angles of these hydrogen bonds.

Panel (A) focuses on the hydrogen bonds within the inorganic 1D chain. The blue lines depict hydrogen bonds acting as a bridge between two parallel chains, reinforcing the cohesion between them. Additionally, red lines highlight the interactions between the oxygen atoms from both chains and chlorine atoms, strengthening the intra-chain connectivity and contributing to the rigidity of the framework.

Panel (B) emphasizes the hydrogen bonding between the organic molecules and the two parallel inorganic chains. The figure highlights how the organic cations interact directly with the inorganic framework, forming hydrogen bonds that further stabilize the 1D structure. This connectivity suggests that the organic molecules are not merely spacers but actively participate in the stabilization of the crystalline architecture.

Panel (C) showcases halogen–halogen interactions within the structure, which occur between chlorine atoms. These interactions add another layer of stability, helping to fine-tune the packing arrangement of the inorganic chains. Halogen–halogen contacts are known to play a significant role in modulating the electronic properties of materials, indicating that these subtle yet crucial interactions may impact the compound's optoelectronic behavior.

Fig. 5 provides a detailed visualization of the π-interactions within the Pd-based hybrid perovskite structure, highlighting their crucial role in supramolecular organization and stability. The top representation showcases the complete set of π-interactions present within the system, while the three subfigures (A, B, and C) isolate each interaction type for clarity.

Panel A, occur between aromatic rings of adjacent organic cations with centroid-to-centroid distances ranging from 3.59 to 3.81 Å. These distances fall within the optimal range reported

for effective π–π overlap, facilitating electronic coupling that can enhance charge transport and exciton migration along the organic layers. Such interactions are well documented in related metal-halide perovskites, where they improve optical properties and contribute to material robustness.[23,24]

Panel B illustrates N–H⋯π interactions, where the hydrogen atoms of ammonium groups engage with the π-electron clouds of aromatic rings at distances around 3.58 to 3.85 Å. These interactions form critical bridges linking hydrogen bonding networks with aromatic stacking, thereby integrating the organic and inorganic components into a cohesive supramolecular framework. Comparable N–H⋯π bonding has been reported to influence mechanical stability and electronic characteristics in hybrid perovskites.[25]

Finally, Panel C highlights C–H⋯π interactions with longer contact distances (3.66 to 3.99 Å). Although weaker than π–π and N–H⋯π interactions, these contribute to fine-tuning the packing efficiency and ensuring tight molecular packing, which is essential for thermal stability and charge mobility. Together, these π-interactions create a multidimensional network that underpins the material's mechanical integrity and optoelectronic performance. In comparison to previously studied Pd-based hybrid perovskites such as $[(CH_3)_2NH_2]_2PdBr_4$ and $(CH_3NH_3)_2PdCl_4$, where π-interactions are less prominent or more symmetrical due to higher structural symmetry.[26,27] The asymmetric unit with $Z' = 2$ in our compound allows for a richer variety of π-interactions, potentially enhancing anisotropic charge transport and providing opportunities for tuning electronic and optical properties through molecular design.

Vibrational studies

The Raman spectrum (Fig. 6) of $(C_9H_8N)[PdCl_3(H_2O)]$ displays a series of well-defined vibrational peaks characteristic of both the organic cation and the inorganic coordination environment. In the high-wavenumber region, the most prominent feature appears at 1653 cm^{-1}, which is attributed to the $\nu(C=N)$ stretching mode of the heteroaromatic ring. This value is in good agreement with previously reported pyridyl-based hybrid perovskites, confirming the integrity of the aromatic framework upon coordination. The peak observed at 1386 cm^{-1} corresponds to the $\nu(C–N)$ stretching vibration, further supporting the preservation of the organic cation's structure. In the lower frequency region, the signal at 773 cm^{-1} is assigned to $\delta(Pd–Cl)$ bending, while the band at 518 cm^{-1} is associated with $\beta(Pd–O–Cl)$ deformation, providing evidence for the coordination of water molecules to Pd(II). Notably, very low-frequency bands at 82 cm^{-1} and 44 cm^{-1} correspond to lattice modes, indicating a crystalline and well-ordered solid. The absence of significant shifts in the metal-ligand bands compared to similar Pd(II) halide complexes suggests that the square-planar coordination environment is retained without major distortion.

The IR transmittance (Fig. 7) spectrum complements the Raman analysis by highlighting vibrational modes that are IR-active but Raman-inactive, thus providing a complete picture of the compound's vibrational landscape. A broad absorption at 3408 cm^{-1} corresponds to $\nu(O–H)$ stretching from coordinated

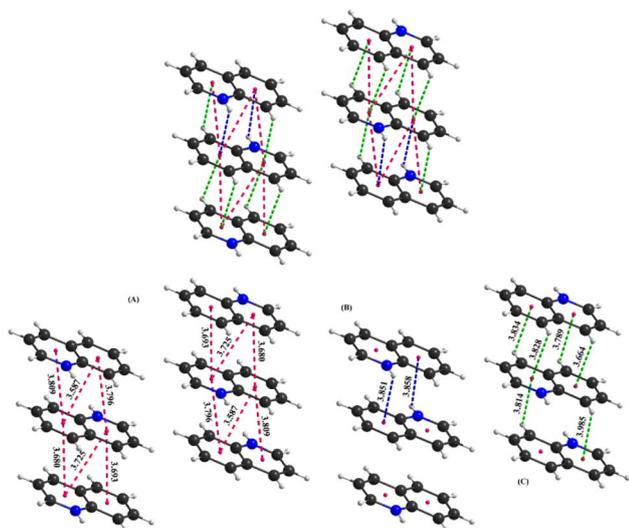Fig. 5 The intricate network of hydrogen bonds within the perovskite crystal lattice.

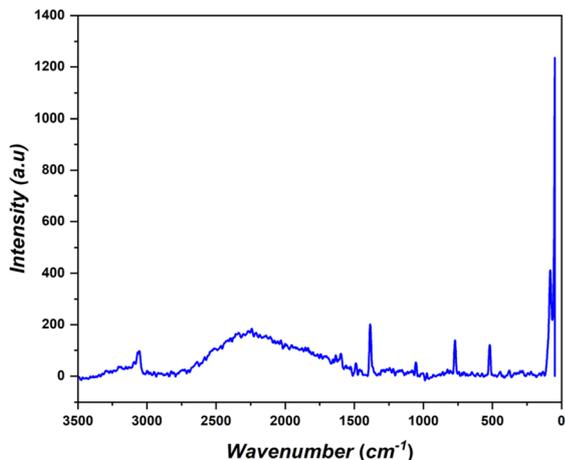Fig. 6 Raman spectrum of $(C_9H_8N)[PdCl_3(H_2O)]$.

Fig. 7 Infrared spectrum of $(C_9H_8N)[PdCl_3(H_2O)]$.

Fig. 8 Simultaneous TGA-DSC curves for the decomposition of $(C_9H_8N)[PdCl_3(H_2O)]$.

water molecules, indicative of hydrogen bonding within the lattice.[28] The bands at 3058 cm^{-1} and 2681 cm^{-1} are assigned to νas(C–H) and ν(N–H) stretching modes, confirming the presence of the organic moiety. In the fingerprint region, a strong absorption at 1600 cm^{-1} is assigned to ν(C=N) stretching, consistent with aromatic heterocycles, while the band at 1550 cm^{-1} corresponds to ν(C=C) aromatic ring stretching.[29] Additional absorptions at 1383 cm^{-1} and 1299 cm^{-1} are assigned to ν(C–N) and in-plane ring vibrations, respectively. Importantly, the 1053 cm^{-1} band corresponds to ν(Pd–O), confirming coordination of water to the palladium center. The metal-halide region shows distinctive peaks at 943 cm^{-1} (ν(Pd–Cl)), 810 cm^{-1} (δ(framework)), 615 cm^{-1} (νas(Pd–Cl)), and 523 cm^{-1} (β(Pd–O–Cl)), all consistent with literature values for Pd(II) chloride complexes.

The combined Raman and IR characterizations confirm the coexistence of the organic cation ($C_9H_8N^+$) and the inorganic $[PdCl_3(H_2O)]^-$ moiety, verifying the successful synthesis of the hybrid material.[30] The clear observation of ν(Pd–O) and ν(Pd–Cl) vibrations, along with corresponding deformation modes, provides strong evidence for the anticipated square-planar coordination geometry around Pd(II).[31] The aromatic ν(C=N) and ν(C–N) modes confirm that the organic cation remains structurally intact during synthesis, while the broad ν(O–H) band indicates the presence of hydrogen bonding, which may influence the thermal and structural stability of the hybrid lattice.[32] The persistence of sharp lattice modes in the low-frequency region supports a highly ordered crystalline framework, which is desirable for maintaining electronic and optical properties. These vibrational findings, when correlated with X-ray diffraction data, not only validate the proposed crystal structure but also underscore the robustness of the Pd-ligand bonding environment—an essential factor for the material's stability and performance in electrochemical applications such as the electro-Fenton process.

Thermal study

Thermal analysis of $(C_9H_8N)[PdCl_3(H_2O)]$ was conducted to evaluate the compound's stability and decomposition pathway in correlation with its crystallographic features. The thermogravimetric (TGA) profile exhibits four main weight-loss steps, each supported by distinct thermal events in the differential scanning calorimetry (DSC) curve are shown in Fig. 8.
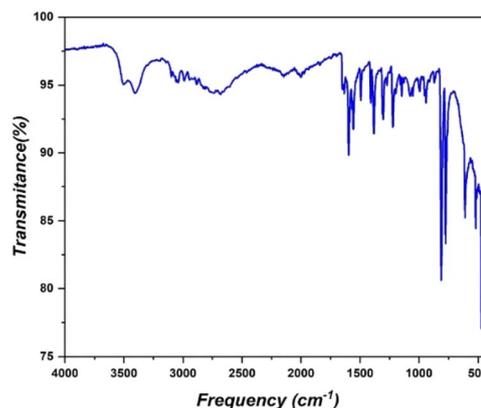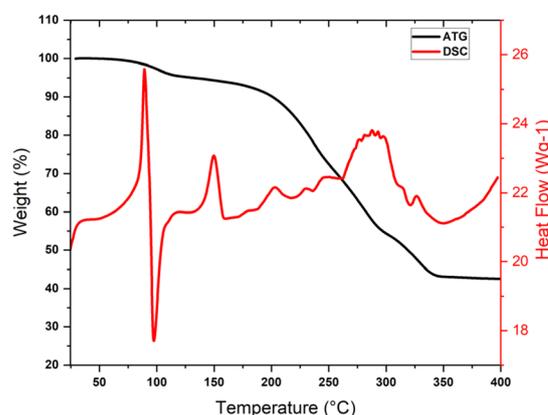
The first mass loss occurs between 75–125 °C and is attributed to the release of two coordinated water molecules (~4.6% experimental), consistent with the weak Pd–O bonds observed in the structure. This step is supported by an exothermic peak followed by a minor endothermic transition in the DSC, reflecting bond dissociation and water desorption.

The second stage (125–250 °C) corresponds to the partial degradation of the organic cation and the release of Cl_2. This process involves cleavage of Pd–Cl bonds and initial breakdown of the quinoline backbone, in agreement with the compound's asymmetric $PdCl_3(H_2O)$ geometry. A comparable decomposition behavior was reported in Pd(DABA)Cl_2 complexes, where coordinated chloride and nitrogen-donor ligands are eliminated in successive stages, leading to Pd residue formation.[33]

A third exothermic event (250–300 °C) matches the release of remaining chloride ligands and further disruption of the coordination environment. The consistency between theoretical and experimental weight loss confirms the stepwise nature of the

degradation. This behavior is also consistent with findings in Pd(acac)$_2$, where palladium-organic complexes undergo progressive ligand loss under thermal stress before stabilizing as metallic Pd.[34]

The final decomposition phase (300–350 °C) involves combustion of the remaining organic framework and residue stabilization, likely forming a Pd-carbon-based product. The plateau above 350 °C suggests the formation of a thermally stable residual phase.

Overall, the TGA/DSC results directly reflect structural features such as weakly bound ligands, coordination asymmetry, and organic backbone stability. This thermal behavior is consistent with previously reported thermolysis pathways in related Pd(II) complexes, further validating the decomposition model proposed for $(C_9H_8N)[PdCl_3(H_2O)]$.

Electro-Fenton performance in paraquat degradation

Effect of operational parameters. The electro-Fenton process was systematically investigated for the degradation of paraquat using chemical oxygen demand as a primary indicator of mineralization. The experimental system employed a boron-doped diamond anode, and a glassy carbon electrode (GCE) modified with a Pd-based hybrid perovskite complex, forming a synergistic platform for advanced oxidation.

The influence of key operational parameters pH, Fe^{2+} concentration, current density, and supporting electrolyte was explored to optimize process performance and elucidate mechanistic aspects (Fig. 9).

Among all tested parameters, the initial pH had the most pronounced effect on COD removal efficiency. Maximum degradation was achieved at pH 3, which favors the classical Fenton reaction wherein Fe^{2+} catalyzes the decomposition of electrochemically generated hydrogen peroxide into highly reactive hydroxyl radicals, as described by the reaction:[29]

$$Fe^{2+} + H_2O_2 \rightarrow Fe^{3+} + {}^\bullet OH + OH^-$$

At higher pH values (>5), the precipitation of Fe^{3+} as Fe(OH)$_3$ impairs the availability of iron ions, thereby reducing the

generation of $^\bullet$OH radicals. These results are in line with previous reports indicating that acidic conditions are essential for sustaining the Fenton cycle and promoting effective mineralization.

Once pH was fixed at 3, the effect of varying Fe^{2+} concentrations was examined. An optimal value of 0.2 mM was identified, beyond which a decrease in COD removal was observed. This decline is likely due to the scavenging of $^\bullet$OH radicals by excess Fe^{2+}, forming Fe^{3+} and OH$^-$, a reaction that competes with pollutant oxidation. Interestingly, the modified Pd-GCE cathode facilitated a more efficient regeneration of Fe^{2+} from Fe^{3+}, enhancing the continuity of the Fenton cycle compared to the unmodified electrode. This improvement is attributed to the conductive and redox-active nature of the perovskite coating, which enhances electron transfer and catalytic performance at the cathode surface.[35] This interpretation is further supported by the catalytic literature, where palladium sites are widely recognized for facilitating the Fe^{3+} → Fe^{2+} redox transition under acidic electro-Fenton conditions.[12] The consistently higher COD and TOC removal efficiencies obtained with the Pd-GCE at relatively low current densities indirectly confirm this role, as the system maintained a steady Fe^{2+} pool without requiring excessive energy input. Such Pd-assisted regeneration of Fe^{2+} sustains the Fenton cycle more effectively, ensuring continuous hydroxyl radical production and ultimately accelerating pollutant mineralization.

The applied current density also played a crucial role, as it governs the rate of H$_2$O$_2$ production and the regeneration of Fe^{2+}. A current density of 20 mA cm^{-2} was found to be optimal, providing sufficient driving force for H$_2$O$_2$ generation through the cathodic reduction of oxygen:[36]

$$O_2 + 2H^+ + 2e^- \rightarrow H_2O_2$$
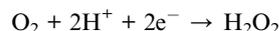
Exceeding this value led to diminished efficiency, likely due to parasitic side reactions such as the further reduction of H$_2$O$_2$ or oxygen directly to water. The BDD anode was particularly beneficial under these conditions, as its high overpotential for oxygen evolution and chemical inertness enabled the generation of physisorbed hydroxyl radicals (BDD($^\bullet$OH)) without electrode passivation. This added an important heterogeneous oxidation pathway that complemented the homogeneous Fenton mechanism occurring in the bulk solution.

The nature of the supporting electrolyte was also significant in shaping the degradation pathway. Sodium sulfate (Na$_2$SO$_4$) exhibited superior performance compared to sodium chloride (NaCl) and sodium nitrate (NaNO$_3$). While Na$_2$SO$_4$ maintained stable ionic conductivity without generating reactive intermediates, NaCl introduced active chlorine species through anodic oxidation of Cl$^-$ ions, followed by hydrolysis to form hypochlorous acid (HOCl), as follows:[37]
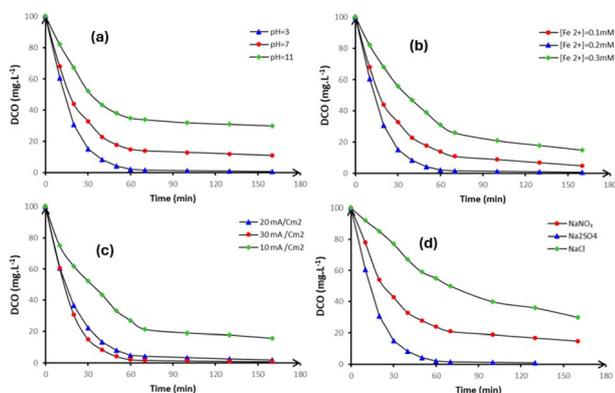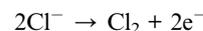
$$2Cl^- \rightarrow Cl_2 + 2e^-$$

$$Cl_2 + H_2O \rightarrow HOCl + H^+ + Cl^-$$

Fig. 9 Effect of operational parameters on COD removal efficiency during electro-Fenton degradation of paraquat: (a) initial pH, (b) Fe^{2+} concentration, (c) current density, (d) supporting electrolyte.

These species may act as oxidants, but they also pose environmental risks due to the potential formation of chlorinated by-products. Hence, the use of Na_2SO_4 ensured that oxidation was primarily governed by ·OH radicals and remained environmentally benign.

Collectively, the results demonstrate that optimal operational conditions pH 3, 0.2 mM Fe^{2+}, 20 mA cm^{-2}, and Na_2SO_4 maximize the efficiency of the electro-Fenton process. Under these settings, the synergistic use of a BDD anode and a Pd-based hybrid perovskite-modified cathode significantly enhanced COD removal compared to conventional setups, validating the effectiveness of combining advanced electrode materials with carefully tuned operational parameters for sustainable pollutant degradation.

Beyond these optimized conditions, it is noteworthy that the Pd-GCE cathode maintained its high performance throughout the entire electrolysis period without any observable decline in COD or TOC removal efficiency. This consistent behavior, combined with the known chemical robustness of Pd-based surfaces, strongly indicates that the hybrid coating exhibits excellent operational stability under prolonged EF operation, supporting its suitability for practical water treatment applications.

Comparative degradation of paraquat by different advanced oxidation processes. To evaluate the relative effectiveness of different advanced oxidation processes in degrading paraquat herbicide, a comparative study was conducted using four representative techniques: anodic oxidation, normal electro-Fenton, Pd-based hybrid perovskite-enhanced electro-Fenton, and photodegradation. The evaluation was based on the evolution of paraquat concentration and total organic carbon over time, as well as the final removal efficiencies (Fig. 10). The Pd-based electro-Fenton system exhibited the fastest and most

complete degradation, achieving near-complete mineralization of paraquat within 180 minutes.

This superior performance is attributed to the combined effect of the boron-doped diamond anode, which generates non-selective physisorbed ·OH radicals, and the Pd-based perovskite-modified cathode, which efficiently produces H_2O_2 and regenerates Fe^{2+}. Together, these electrodes establish a dual-path oxidation mechanism involving both homogeneous and heterogeneous radical species.

In comparison, the normal electro-Fenton process achieved slightly lower removal efficiencies, primarily due to the limited activity of the unmodified GCE cathode, which produces lower amounts of H_2O_2 and exhibits slower Fe^{3+} reduction. Anodic oxidation alone, although effective in degrading paraquat through direct oxidation and BDD-mediated ·OH generation, lacked the radical amplification provided by the Fenton cycle. Meanwhile, photodegradation under identical conditions showed the lowest performance, consistent with the known photostability of paraquat and its resistance to UV-based processes.

The bar chart (Fig. 10c) further confirms these findings, showing that the Pd-based electro-Fenton system achieved the highest removal efficiencies for both TOC and paraquat concentration ($\approx 95\%$), significantly surpassing the other methods. These results highlight the technical potential of combining innovative electrode materials with optimized electro-Fenton conditions to address the degradation of persistent organic pollutants.

For context, the performance of the Pd-based hybrid perovskite-modified GCE was compared with that of representative EF cathodes reported in the literature, including Fe–N–C composites, carbon felt, and Pt-based materials. These systems generally achieve TOC removal efficiencies of 70–85% after 3–5 hours of treatment under similar conditions. In contrast, the Pd-GCE achieved nearly 95% TOC removal within 180 minutes at a lower current density, reflecting the catalytic advantage of the Pd redox sites and the conductive perovskite coating in accelerating H_2O_2 production and Fe^{3+}/Fe^{2+} cycling, thereby enabling faster and more complete pollutant mineralization.

Identification and evolution of intermediates. Understanding the formation and degradation of intermediate by-products is essential for elucidating the reaction mechanism and evaluating the environmental safety of the electrochemical treatment process. In many cases, these transient compounds can exhibit significant toxicity, underscoring the importance of monitoring their evolution throughout the treatment period.[38]

During the electro-Fenton degradation of paraquat using a boron-doped diamond anode and a Pd-based hybrid perovskite-modified cathode, several aromatic intermediates were identified by HPLC analysis. These included mono-pyridone, 4-carboxy-1-methylpyridinium, and 4,4'-bipyridyl, all of which are typical oxidation products resulting from electrophilic attacks by hydroxyl radicals on the heterocyclic pyridinium rings of paraquat.

As illustrated in Fig. 11, the concentration profiles of these intermediates followed a transient behavior, characterized by a sharp increase during the first 30–60 minutes of electrolysis,
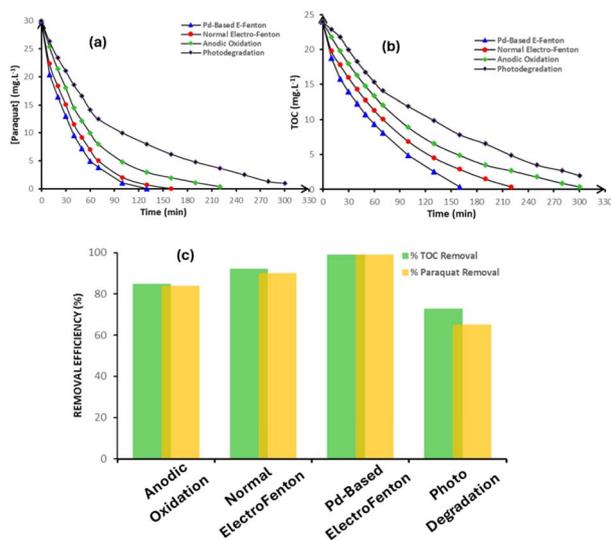

Fig. 10 Paraquat concentration decay (a) and TOC reduction (b) over time by advanced oxidation processes; (c) comparative removal efficiencies.
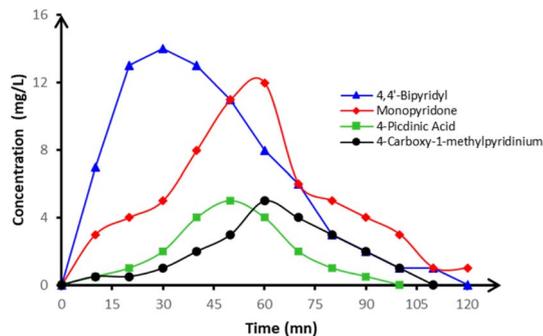
Fig. 11 Time evolution of paraquat and its aromatic degradation intermediates detected during EF process: BDD anode, GCE modified cathode, pH 3.0, [paraquat]$_0$ = 30 mg L^{-1}, J = 20 mA cm^{-2} [H$_2$O$_2$]$_0$ = 20 mM and [Fe^{2+}]$_0$ = 0.2 mM.
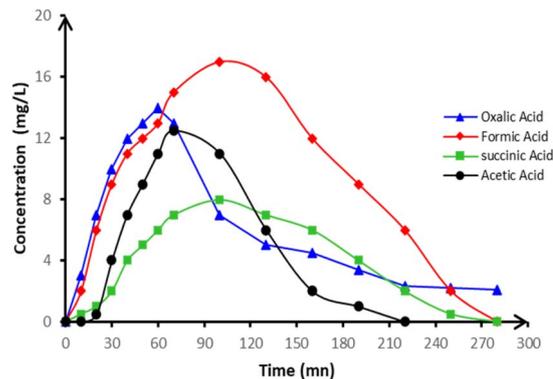

Fig. 12 Time-course of the concentration of relevant carboxylic acids detected during EF process: BDD anode, GCE modified cathode, pH 3.0, [paraquat]$_0$ = 30 mg L^{-1}, J = 20 mAcm^{-2} [H$_2$O$_2$]$_0$ = 20 mM and [Fe^{2+}]$_0$ = 0.2 mM.

corresponding to the active phase of molecular cleavage and rearrangement. Among them, monopyridone exhibited the highest peak concentration, reflecting its role as a primary intermediate, while bipyridyl and carboxypyridinium appeared slightly later, suggesting sequential oxidative steps. This temporal evolution is consistent with proposed degradation pathways in the literature,[39] where paraquat is progressively oxidized through stepwise N-demethylation, ring hydroxylation, and bond cleavage.

Following the peak phase, the concentration of all detected intermediates declined steadily, indicating further oxidation into lower molecular weight compounds. By 120 minutes, the intermediates were nearly undetectable, suggesting their conversion into non-aromatic carboxylic acids and eventually into carbon dioxide and water. This behavior reflects a typical two-stage mineralization mechanism: the first dominated by structural fragmentation of the parent molecule, and the second by gradual breakdown of the resulting intermediates.

The transient accumulation and subsequent disappearance of these species confirm that the electro-Fenton system, under optimized conditions, is capable not only of degrading paraquat but also of minimizing the persistence of potentially hazardous intermediates. These findings validate the efficacy and safety of the process and provide valuable insights into the design of more selective and complete oxidation systems for herbicide-contaminated effluents.

In the later stages of paraquat degradation, once the aromatic rings were broken down, the formation of low-molecular-weight carboxylic acids became prominent. As shown in Fig. 12, several short-chain organic acids including oxalic, formic, acetic, and succinic acids were identified and monitored to assess the progression toward complete mineralization. These compounds are well-established as final intermediates in the oxidative degradation of nitrogen-containing heterocycles.

The evolution profiles revealed distinct behaviors among the detected acids. Formic and acetic acids exhibited a rapid increase in concentration, peaking between 60 and 120 minutes of electrolysis. Their transient accumulation reflects their formation from the oxidation of ring fragments and other

primary intermediates. However, both acids gradually diminished in concentration after their peak, indicating their successful breakdown in the presence of ˙OH radicals and other reactive species generated by the electro-Fenton system. This agrees with previous reports by Rabaaoui *et al.*, who observed similar dynamics in the electrochemical treatment of persistent organic contaminants.[40]

Oxalic acid, by contrast, showed a more persistent behavior. Its concentration increased steadily and reached a plateau of around 60–90 minutes, after which it declined only slowly throughout the remaining treatment time. This trend suggests that oxalic acid is more resistant to direct attack by hydroxyl radicals, consistent with its known stability under oxidative conditions. Similar behavior has been reported in other electrochemical degradation studies, where oxalic acid often represents the final bottleneck before full mineralization. The presence and evolution of these acids reinforce the two-stage degradation mechanism previously observed: an initial fragmentation and formation of aromatic intermediates, followed by their progressive oxidation into simpler aliphatic acids, which eventually mineralize to CO$_2$ and H$_2$O. The persistence of certain acids, particularly oxalic acid, highlights the importance of maintaining adequate oxidant production, especially in the later stages of electrolysis to ensure complete conversion and environmental safety of the treated effluent.

Further confirmation of the near-complete mineralization of paraquat is provided by the monitoring of inorganic nitrogen species released during electrolysis. As shown in Fig. 13, the concentrations of ammonium (NH$_4^+$) and nitrate (NO$_3^-$) steadily increased throughout the 300 minute treatment period, reflecting the progressive cleavage of nitrogen-containing functional groups from the herbicide's molecular structure.

Ammonium levels increased more prominently, reaching a final concentration of approximately 9.8 mg L^{-1}, compared to 5.1 mg L^{-1} for nitrate. This pattern suggests that reduction pathways favoring NH$_4^+$ formation were predominant under the applied electrochemical conditions. The cathodic environment, particularly enhanced by the Pd-based perovskite-modified
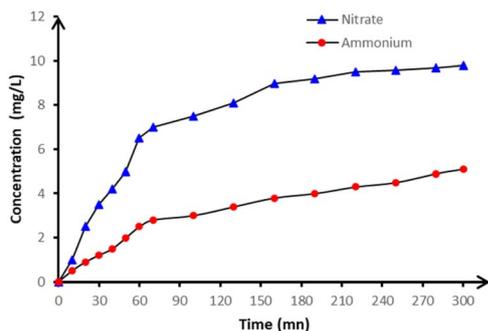
Fig. 13 Accumulation of nitrate (▲) and ammonium (●) ions detected during EF process: BDD anode, GCE modified cathode, pH 3.0, $[paraquat]_0 = 30$ mg L^{-1}, $J = 20$ mA cm^{-2} $[H_2O_2]_0 = 20$ mM and $[Fe^{2+}]_0 = 0.2$ Mm.

GCE, likely promoted such reductive transformations. These findings are consistent with those of Martínez-Huitle *et al.*, who reported preferential ammonium formation over nitrate in electrochemical advanced oxidation processes involving nitrogen-rich contaminants.[41] The accumulation of these inorganic ions corroborates the breakdown of paraquat into small, stable end-products. Alongside the evolution of aromatic intermediates and carboxylic acids, the presence of NH_4^+ and NO_3^- represents the final stage in the mineralization pathway. The gradual but sustained formation of these ions confirms that both the organic nitrogen backbone and its substituent groups underwent complete oxidative transformation.

Collectively, the evidence from organic intermediates, low-molecular-weight acids, and released inorganic species establishes a coherent and complete picture of paraquat degradation under the studied conditions. The combination of BDD anode-driven oxidation and Pd-based EF catalysis proves highly effective not only in degrading the parent compound but also in pushing the reaction toward full mineralization, ensuring both performance and environmental safety.

Reaction sequence for paraquat degradation. The degradation mechanism of paraquat under the optimized electro-Fenton system was elucidated by tracking the evolution of organic and inorganic intermediates, leading to a proposed reaction sequence illustrated in Fig. 14. The process begins with the electrophilic attack of hydroxyl radicals generated both homogeneously *via* the Fenton reaction and heterogeneously at the surface of the boron-doped diamond anode. These radicals rapidly target the aromatic pyridinium rings of paraquat, initiating hydroxylation and oxidative N-demethylation. This leads to the formation of several transient intermediates, such as monopyridone, 4-carboxy-1-methylpyridinium, 4-picolinic acid, and 4,4′-bipyridyl, which were experimentally identified through HPLC and confirmed by reference standards.

As oxidation progresses, the aromatic intermediates undergo ring-opening and subsequent degradation into aliphatic acids. Notably, succinic acid, oxalic acid, formic acid, and acetic acid were identified and tracked as typical low-molecular-weight carboxylic acids arising from extensive oxidation. Among them, formic and acetic acids accumulated transiently before declining, suggesting active mineralization. Oxalic acid,
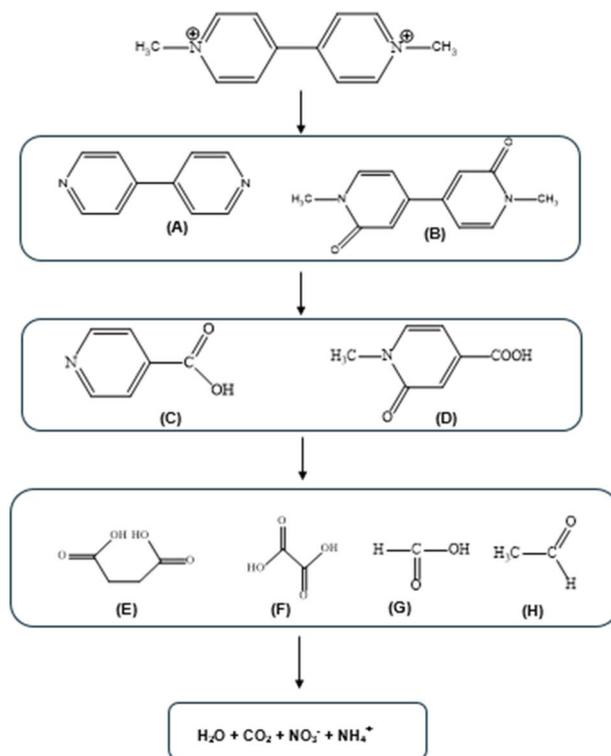

Fig. 14 Proposed reaction pathway for the mineralization of paraquat in aqueous acid medium by hydroxyl radicals generated in the EF process.

however, showed more persistence, indicating its relative resistance to oxidative attack and the need for sustained generation of oxidants in the later stages of the process.

In parallel, the release of nitrogen species such as ammonium and nitrate confirms the breakdown of the nitrogenous moieties of paraquat. Ammonium was the dominant form, likely favored by the reducing environment at the Pd-based cathode, consistent with trends observed in the electrochemical oxidation of other nitrogen-containing compounds. These findings indicate that the degradation follows a two-phase mechanism: an initial stage dominated by the fragmentation of the parent molecule into aromatic and nitrogenous intermediates, and a second phase involving the oxidation of carboxylic acids and conversion of nitrogen groups into their inorganic forms.

The proposed pathway underscores the synergistic role of the advanced electrode materials: the BDD anode provides a high-overpotential surface for ˙OH generation and direct oxidation, while the Pd-based hybrid perovskite cathode facilitates efficient H_2O_2 production and Fe^{2+} regeneration, ensuring continuous radical availability. This dual mechanism not only accelerates degradation but also pushes the process toward full mineralization, offering an effective and environmentally safe strategy for the treatment of paraquat and other persistent organic pollutants.

Conclusion

This study presents the design, synthesis, and comprehensive characterization of a novel one-dimensional palladium-based

hybrid perovskite, $(C_9H_8N)[PdCl_3(H_2O)]$, distinguished by its crystallographic asymmetry and structurally integrated non-covalent interactions. These features were shown to enhance both the structural integrity and functional performance of the material. When employed as a cathodic modifier in a boron-doped diamond-assisted electro-Fenton system, the compound exhibited efficient and sustained catalytic activity toward the degradation of paraquat, highlighting its potential for environmental remediation.

Importantly, this work bridges a critical gap in the current literature by demonstrating how low-dimensional Pd-based hybrid materials can be rationally designed for real-world electrochemical applications. The findings not only under-score the versatility of such frameworks but also suggest new avenues for the integration of structurally engineered perov-skites into advanced oxidative processes. Future investigations will focus on expanding the pollutant scope, probing long-term stability, and further elucidating the mechanistic underpin-nings of the observed catalytic behavior.

Author contributions

Houyem Khlifi: formal analysis, writing – original draft; Ahlem Guesmi: formal analysis, validation Nejmeddine Rabaaoui: investigation, formal analysis; Mourad Cherif: software, inves-tigation; Noureddine Mhadhbi: formal analysis, validation; Wesam Abd El-Fattah: investigation, validation; Naoufel Ben Hamadi: methodology, conceptualization; Houcine Naïli: supervision, review & editing, validation.

Conflicts of interest

The authors declare that they have no known competing financial interests or personal relationships that could have appeared to influence the work reported in this paper.

Data availability

The data that supported the findings of this study were available upon reasonable request.[42]

CCDC 2444206 contains the supplementary crystallographic data for this paper.

The supplementary information file provides additional experimental details, including full crystallographic data (CIF), spectroscopic data (Raman and IR spectra), thermal analysis results, electrochemical characterization, as well as supple-mentary figures and tables supporting the findings of the manuscript. See DOI: https://doi.org/10.1039/d5ra03275j.

Funding

Notes and references

1 Z. Shen, D. Grüner, M. Eriksson, L. M. Belova, C.-W. Nan and H. Yan, Ordered coalescence of nano-crystals in alkaline niobate ceramics with high remanent polarization, *J. Mater.*, 2017, **3**, 267–272, DOI: 10.1016/j.jmat.2017.08.004.

2 E. I. Marchenko, S. A. Fateev, E. A. Goodilin and A. B. Tarasov, Band Gap and Topology of 1D Perovskite-Derived Hybrid Lead Halide Structures, *Crystals*, 2022, **12**, 657, DOI: 10.3390/cryst12050657.

3 X. Liu, Y. Wang, Y. Wang, Y. Zhao, J. Yu, X. Shan, Y. Tong, X. Lian, X. Wan, L. Wang, P. Tian and H.-C. Kuo, Recent advances in perovskites-based optoelectronics, *Nanotechnol. Rev.*, 2022, **11**, 3063–3094, DOI: 10.1515/ntrev-2022-0494.

4 K. Chen, S. Schünemann, S. Song and H. Tüysüz, Structural effects on optoelectronic properties of halide perovskites, *Chem. Soc. Rev.*, 2018, **47**, 7045–7077, DOI: 10.1039/C8CS00212F.

5 K. Du, Q. Tu, X. Zhang, Q. Han, J. Liu, S. Zauscher and D. B. Mitzi, Two-Dimensional Lead(II) Halide-Based Hybrid Perovskites Templated by Acene Alkylamines: Crystal Structures, Optical Properties, and Piezoelectricity, *Inorg. Chem.*, 2017, **56**, 9291–9302, DOI: 10.1021/acs.inorgchem.7b01094.

6 S. Wang, M. Mandal, H. Zhang, D. W. Breiby, O. Yildiz, Z. Ling, G. Floudas, M. Bonn, D. Andrienko, H. I. Wang, P. W. M. Blom, W. Pisula and T. Marszalek, Odd–Even Alkyl Chain Effects on the Structure and Charge Carrier Transport of Two-Dimensional Sn-Based Perovskite Semiconductors, *J. Am. Chem. Soc.*, 2024, **146**, 19128–19136, DOI: 10.1021/jacs.4c03936.

7 A. Negi, L. Yan, C. Yang, Y. Yu, D. Kim, S. Mukherjee, A. H. Comstock, S. Raza, Z. Wang, D. Sun, H. Ade, Q. Tu, W. You and J. Liu, Anomalous Correlation between Thermal Conductivity and Elastic Modulus in Two-Dimensional Hybrid Metal Halide Perovskites, *ACS Nano*, 2024, **18**, 14218–14230, DOI: 10.1021/acsnano.3c12172.

8 M. A. Kuddus Sheikh, F. Maddalena, D. Kowal, M. Makowski, S. Mahato, R. Jedrzejewski, R. Bhattarai, M. E. Witkowski, K. J. Drozdowski, W. Drozdowski, C. Dang, T. D. Rhone and M. D. Birowosuto, Effect of Dual-Organic Cations on the Structure and Properties of 2D Hybrid Perovskites as Scintillators, *ACS Appl. Mater. Interfaces*, 2024, **16**, 25529–25539, DOI: 10.1021/acsami.4c01741.

9 M. Morana, W. Kaiser, R. Chiara, B. Albini, D. Meggiolaro, E. Mosconi, P. Galinetto, F. De Angelis and L. Malavasi, Origin of Broad Emission Induced by Rigid Aromatic Ditopic Cations in Low-Dimensional Metal Halide Perovskites, *J. Phys. Chem. Lett.*, 2023, **14**, 7860–7868, DOI: 10.1021/acs.jpclett.3c01872.

10 F. J. Iftikhar, Q. Wali, S. Yang, Y. Iqbal, R. Jose, S. Munir, I. A. Gondal and M. E. Khan, Structural and optoelectronic properties of hybrid halide perovskites for solar cells, *Org. Electron.*, 2021, **91**, 106077, DOI: 10.1016/j.orgel.2021.106077.

11 A. Garrote-Márquez, L. Lodeiro, R. Suresh, N. Cruz Hernández, R. Grau-Crespo and E. Menéndez-Proupin, Hydrogen Bonds in Lead Halide Perovskites: Insights from Ab Initio Molecular Dynamics, *J. Phys. Chem. C*, 2023, **127**, 15901–15910, DOI: **10.1021/acs.jpcc.3c02376**.

12 H.-S. Bae, M. A. Mahadik, Y.-S. Seo, W. S. Chae, H.-S. Chung, H. I. Ryu, M. Cho, P. J. Shea, S. H. Choi and J. S. Jang, Palladium metal oxide/hydroxide clustered cobalt oxide co-loading on acid treated TiO2 nanorods for degradation of organic pollutants and Salmonella typhimurium inactivation under simulated solar light, *Chem. Eng. J.*, 2021, **408**, 127260, DOI: **10.1016/j.cej.2020.127260**.

13 A. B. Buer, N. Y. A. Boateng, B. Asafo-Adjei, S. Kwon and J. W. Jo, Recent progress in the development of metal halide perovskite electronics for sensing applications, *Mater. Today Electron.*, 2024, **10**, 100122, DOI: **10.1016/j.mtelec.2024.100122**.

14 M. Tang, S. Zhu, Z. Liu, C. Jiang, Y. Wu, H. Li, B. Wang, E. Wang, J. Ma and C. Wang, Tailoring π-Conjugated Systems: From π–π Stacking to High-Rate-Performance Organic Cathodes, *Chem*, 2018, **4**, 2600–2614, DOI: **10.1016/j.chempr.2018.08.014**.

15 S. Abdolahi Jonghani, Z. Biglari and A. Gholipour, NMR investigation of substituent effects on strength of π-π stacking and hydrogen bonding interactions to supports the formation of [2 + 2] photodimerization in (para-X-ba):::(bpe)‖(bpe):::(para-X-ba) complexes, *Arab. J. Chem.*, 2020, **13**, 6395–6402, DOI: **10.1016/j.arabjc.2020.05.040**.

16 C. S. Hansen, S. J. Blanksby and A. J. Trevitt, Ultraviolet photodissociation action spectroscopy of gas-phase protonated quinoline and isoquinoline cations, *Phys. Chem. Chem. Phys.*, 2015, **17**, 25882–25890, DOI: **10.1039/C5CP02035B**.

17 R. F. Fernandes, P. H. F. Stroppa, G. R. Ferreira, A. D. da Silva, H. G. M. Edwards and L. F. C. de Oliveira, Vibrational spectroscopic study of some quinoline derivatives, *Vib. Spectrosc.*, 2016, **86**, 128–133, DOI: **10.1016/j.vibspec.2016.06.005**.

18 S. R. Majeed, M. A. Amin, F. A. Attaby, M. E. Alberto and A. A. Soliman, Synthesis, Characterization, Thermal Analysis, DFT, and Cytotoxicity of Palladium Complexes with Nitrogen-Donor Ligands, *Molecules*, 2022, **27**, 964, DOI: **10.3390/molecules27030964**.

19 B. Ben Salah, F. Hajlaoui, K. Karoui, N. Audebrand, T. Roisnel, S. Freslon, N. Zouari and F. Jomni, Exploration of new chiral hybrid semiconducting palladium halide complexes: [(R)/(S)-2-Methylpiperazinediiium]PdCl4, *Mater. Res. Bull.*, 2023, **164**, 112251, DOI: **10.1016/j.materresbull.2023.112251**.

20 S. J. Kim, S. Park, H. M. Cho and H. W. Jang, Low-dimensional halide perovskites for advanced electronics, *Mater. Today Electron.*, 2024, **9**, 100111, DOI: **10.1016/j.mtelec.2024.100111**.

21 F. Brivio, A. B. Walker and A. Walsh, Structural and electronic properties of hybrid perovskites for high-efficiency thin-film photovoltaics from first-principles, *APL Mater.*, 2013, **1**, 042111, DOI: **10.1063/1.4824147**.

22 J. Sun, H. Lu, H. Lin, L. Du, W. Huang, H. Li and T. Cui, Electrochemical oxidation of aqueous phenol at low concentration using Ti/BDD electrode, *Sep. Purif. Technol.*, 2012, **88**, 116–120, DOI: **10.1016/j.seppur.2011.12.022**.

23 K. Trabelsi, N. Drissi, F. Hajlaoui, M. Zighrioui, A. Rhaiem, N. Audebrand, T. Roisnel and K. Karim, [(CH 3) 2 NH 2] 2 PdBr 4 , a layered hybrid halide perovskite semiconductor with improved optical and electrical properties, *RSC Adv.*, 2023, **13**, 23348–23358, DOI: **10.1039/D3RA04085B**.

24 T. J. Huang, Z. X. Thiang, X. Yin, C. Tang, G. Qi and H. Gong, (CH 3 NH 3) 2 PdCl 4 : A Compound with Two-Dimensional Organic–Inorganic Layered Perovskite Structure, *Chem.–A Eur. J.*, 2016, **22**, 2146–2152, DOI: **10.1002/chem.201503680**.

25 D. Duan, C. Ge, M. Z. Rahaman, C.-H. Lin, Y. Shi, H. Lin, H. Hu and T. Wu, Recent progress with one-dimensional metal halide perovskites: from rational synthesis to optoelectronic applications, *NPG Asia Mater.*, 2023, **15**, 8, DOI: **10.1038/s41427-023-00465-0**.

26 M. L. Ball, J. V. Milić and Y.-L. Loo, The Emerging Role of Halogen Bonding in Hybrid Perovskite Photovoltaics, *Chem. Mater.*, 2022, **34**, 2495–2502, DOI: **10.1021/acs.chemmater.1c03117**.

27 J. R. Di Iorio and R. Gounder, Controlling the Isolation and Pairing of Aluminum in Chabazite Zeolites Using Mixtures of Organic and Inorganic Structure-Directing Agents, *Chem. Mater.*, 2016, **28**, 2236–2247, DOI: **10.1021/acs.chemmater.6b00181**.

28 R. M. Ramadan, R. G. Mohamed, M. Hassan and S. M. El-Medani, Spectroscopic and Theoretical Studies of Some Bivalent Metal Complexes of a Quinoline Schiff Base Derivative, *J. Transit. Met. Complexes*, 2020, **3**, 1–11, DOI: **10.32371/jtmc/246114**.

29 R. Golla, P. R. Kumar, P. A. Suchethan, S. Foro and G. Nagaraju, Synthesis, photophysical, electrochemical properties and crystal structures and Hirschfeld surface analysis of 4′-dimethoxyphenyl-(2,6-di-2-pyrazinyl) pyridines, *J. Mol. Struct.*, 2020, **1201**, 127118, DOI: **10.1016/j.molstruc.2019.127118**.

30 A. Nordheider, K. Hüll, J. K. D. Prentis, K. S. Athukorala Arachchige, A. M. Z. Slawin, J. D. Woollins and T. Chivers, Main Group Tellurium Heterocycles Anchored by a P 2 V N 2 Scaffold and Their Sulfur/Selenium Analogues, *Inorg. Chem.*, 2015, **54**, 3043–3054, DOI: **10.1021/acs.inorgchem.5b00161**.

31 B. Sureshkumar, Y. S. Mary, C. Y. Panicker, S. Suma, S. Armaković, S. J. Armaković, C. Van Alsenoy and B. Narayana, Quinoline derivatives as possible lead compounds for anti-malarial drugs: Spectroscopic, DFT and MD study, *Arab. J. Chem.*, 2020, **13**, 632–648, DOI: **10.1016/j.arabjc.2017.07.006**.

32 K. Inoue, Y. Litman, D. M. Wilkins, Y. Nagata and M. Okuno, Is Unified Understanding of Vibrational Coupling of Water Possible? Hyper-Raman Measurement and Machine Learning Spectra, *J. Phys. Chem. Lett.*, 2023, **14**, 3063–3068, DOI: **10.1021/acs.jpclett.3c00398**.

33 A. Rivelli, V. Fitzpatrick, C. Blair, K. Copeland and J. Richards, Incidence of COVID-19 reinfection among

Midwestern healthcare employees, *PLoS One*, 2022, **17**, e0262164, DOI: 10.1371/journal.pone.0262164.

34 B. Janković and S. Mentus, A Kinetic Study of the Nonisothermal Decomposition of Palladium Acetylacetonate Investigated by Thermogravimetric and X-Ray Diffraction Analysis Determination of Distributed Reactivity Model, *Metall. Mater. Trans. A*, 2009, **40**, 609–624, DOI: 10.1007/s11661-008-9754-4.

35 Y. Gong, W. Jia, B. Zhou, K. Zheng, J. Gao, Y. Wu, S. Yu, Y. Xue and Y. Wu, Novel graphite-based boron-doped diamond coated electrodes with refractory metal interlayer for high-efficient electrochemical oxidation degradation of phenol, *Sep. Purif. Technol.*, 2025, **355**, 129550, DOI: 10.1016/j.seppur.2024.129550.

36 N. Rabaaoui, Y. Moussaoui, M. S. Allagui, B. Ahmed and E. Elaloui, Anodic oxidation of nitrobenzene on BDD electrode: Variable effects and mechanisms of degradation, *Sep. Purif. Technol.*, 2013, **107**, 318–323, DOI: 10.1016/j.seppur.2013.01.047.

37 M. E. K. Saad, N. Rabaaoui, E. Elaloui and Y. Moussaoui, Mineralization of p-methylphenol in aqueous medium by anodic oxidation with a boron-doped diamond electrode, *Sep. Purif. Technol.*, 2016, **171**, 157–163, DOI: 10.1016/j.seppur.2016.07.018.

38 A. Ouni, N. Rabaaoui, L. Mechi, N. Enaceur, A. K. D. AlSukaibi, E. M. Azzam, K. M. Alenezi and Y. Moussaoui, Removal of pesticide chlorobenzene by anodic degradation: Variable effects and mechanism, *J. Saudi Chem. Soc.*, 2021, **25**, 101326, DOI: 10.1016/j.jscs.2021.101326.

39 N. Rabaaoui, M. E. K. Saad, Y. Moussaoui, M. S. Allagui, A. Bedoui and E. Elaloui, Anodic oxidation of o-nitrophenol on BDD electrode: Variable effects and mechanisms of degradation, *J. Hazard. Mater.*, 2013, **250–251**, 447–453, DOI: 10.1016/j.jhazmat.2013.02.027.

40 N. Rabaaoui and M. S. Allagui, Anodic oxidation of salicylic acid on BDD electrode: Variable effects and mechanisms of degradation, *J. Hazard. Mater.*, 2012, **243**, 187–192, DOI: 10.1016/j.jhazmat.2012.10.016.

41 C. A. Martínez-Huitle, M. A. Rodrigo, I. Sirés and O. Scialdone, A critical review on latest innovations and future challenges of electrochemical technology for the abatement of organics in water, *Appl. Catal. B Environ.*, 2023, **328**, 122430, DOI: 10.1016/j.apcatb.2023.122430.

42 H. Khlifi, A. Guesmi, N. Rabaaoui, M. Cherif, N. Mhadhbi, W. Abd El-Fattah, N. Ben Hamadi and H. Naïli, CCDC 2444206: Experimental Crystal Structure Determination, 2025, DOI: 10.5517/ccdc.csd.cc2n1dch.